Studies of nanocomposites of carbon nanotubes and a negative dielectric anisotropy liquid crystal

P. Kalakonda, R. Basu, I. R. Nemitz, C. Rosenblatt, and G. S. Iannacchione

Citation: The Journal of Chemical Physics **140**, 104908 (2014); doi: 10.1063/1.4867791
View online: http://dx.doi.org/10.1063/1.4867791
View Table of Contents: http://scitation.aip.org/content/aip/journal/jcp/140/10?ver=pdfcov
Published by the AIP Publishing

Studies of nanocomposites of carbon nanotubes and a negative dielectric anisotropy liquid crystal

P. Kalakonda,[1,2] R. Basu,[3] I. R. Nemitz,[4] C. Rosenblatt,[4] and G. S. Iannacchione[1,a)]
[1]*Department of Physics, Worcester Polytechnic Institute, Worcester, Massachusetts 01609, USA*
[2]*Department of Materials Science and Engineering, Carnegie Mellon University, Pittsburgh, Pennsylvania 15213, USA*
[3]*Department of Physics, The United States Naval Academy, Annapolis, Maryland 21402, USA*
[4]*Department of Physics, Case Western Reserve University, Cleveland, Ohio 44106, USA*

(Received 23 November 2013; accepted 25 February 2014; published online 13 March 2014)

It has been widely recognized that the combination of carbon nanotube (CNT) and liquid crystals (LCs) not only provides a useful way to align CNTs, but also dramatically enhances the order in the LC phases, which is especially useful in liquid crystal display (LCD) technology. As the measure of this phase behavior, the complex specific heat is presented over a wide temperature range for a negative dielectric anisotropy alkoxyphenylbenzoate liquid crystal (9OO4) and CNT composites as a function of CNT concentration. The calorimetric scans were performed under near-equilibrium conditions between 25 and 95 °C, first cooling and then followed by heating for CNT weight percent ranging from $\phi_w = 0$ to 0.2. All 9OO4/CNT mesophases have transition temperatures ∼1 K higher and a crystallization temperature 4 K higher than that of the pure 9OO4. The crystal phase superheats until a strongly first-order specific heat feature is observed, 0.5 K higher than in the pure 9OO4. The transition enthalpy for the nanocomposite mesophases is 10% lower than that observed in the pure 9OO4. The strongly first-order crystallization and melting transition enthalpies are essentially constant over this range of ϕ_w. Complementary electroclinic measurement on a 0.05 wt. % sample, cooling towards the smectic-*C* phase from the smectic-*A*, indicates that the Sm*A*-Sm*C* transition remains mean-field-like in the presence of the CNTs. Given the homogeneous and random distribution of CNTs in these nanocomposites, we interpret these results as arising from the LC-CNT surface interaction pinning the orientational order uniformly along the CNT, without pinning the position of the 9OO4 molecule, leading to a net ordering effect for all phases. These effects of incorporating CNTs into LCs are likely due to "anisotropic orientational" coupling between CNT and LC, the change in the elastic properties of composites and thermal anisotropic properties of the CNTs. © *2014 AIP Publishing LLC*. [http://dx.doi.org/10.1063/1.4867791]

I. INTRODUCTION

Composites of nanoparticles with fluids or complex fluids represent a unique physical system where properties of the components fully or partially mix and new behavior can emerge. Traditional composites are relatively well understood as the superposition, weighted by volume or mass, of the components' properties and the interfacial interactions. As the filler shrinks in size, the surface area comes to dominate, leading to unique behavior of the nanocomposites. Carbon nanotubes (CNTs) and liquid crystals (LCs) are good examples of such components. Both materials are highly anisotropic and long-range orientational order, resulting in macroscopic anisotropies is of great importance. For a large number of applications, a challenge lies in the alignment and ordering of CNTs to take advantages of their highly anisotropic characteristics.

Since their discovery in 1991,[1] carbon nanotubes have emerged as a new class of nanosized particles for incorporation into various liquid crystal systems, attracting considerable interest from both basic science researchers and industry. As a result of the exceptional intrinsic properties of carbon nanotubes, novel materials can be envisioned that exhibit property enhancements, even at CNT concentrations much lower than in conventional composite technology.[2] In the field of thermoplastic nanocomposites, reported property enhancements include improved mechanical performance,[3,4] high thermal and electrical conductivity,[5–7] increased crystallization rate,[8–10] and altered rheological behavior.[11,12] In addition to carbon nanotubes' thermal, mechanical, and magnetic properties,[13–22] their unique electrical character makes them potentially useful materials for use in nanoelectronic devices.[2,23–26]

Liquid crystals[27–29] are anisotropic fluids that exhibit one or more thermodynamically stable phases between an isotropic liquid and a full, three-dimensionally ordered solid. In the nematic (*N*) phase, LCs show long range orientational order. In the smectic-*A* (Sm*A*) phase, the rod-like molecules are arranged in layers with their long axes, on average, normal to the layer planes, and they show both orientational and partial translational order characterized by a quasi-1 D density wave. The smectic phases incorporate structures with diverse symmetry,[30] such as that of smectic-*C* (Sm*C*), in which the director tilts away from the layer. In the smectic-*B* (Sm*B*) phase

a)Electronic mail: gsiannac@wpi.edu

the molecules show short-range hexagonal ordering within the layers but not from layer to layer, and all smectic phases exhibit, at best, quasi-long-range order. Higher-order, lower-symmetry, liquid crystalline materials are studied because of their industrial applications, as well as important physical models of phase ordering and self-assembly.[29,30]

When CNTs are dispersed in a liquid crystal host, they can modify the physical properties, and hence the phase behavior of the nanocomposite. Due to the specific surface anchoring between nanoparticle and LC, the nanoparticles can act either as nucleation sites for a given type of order or as disordering sites that stabilize the isotropic phase.[31,32] However, if the local ordering effect of CNT surfaces is randomly arranged, this can lead to a random-field effect[33] and an overall disordering of the composites. Investigations have been made on liquid crystal nanocomposites using optical microscopy and differential scanning calorimetry (DSC), finding an enhancement of the isotropic to nematic phase transition temperature and revealing a "*chimney − type*" temperature-concentration phase diagram over a narrow range of CNT concentration between 0.001 and 0.002 wt. %.[34] In fact, researchers found that the addition of CNT increases the clearing point of LCs because of the strong attraction of CNT and LC. It also was observed that aligned CNTs can cause an increase of the orientational order in the LC.[41,42] However, other studies have found disordering effects of CNTs on LC phases.[31] Yet other work has shown improved electro-optical switching properties of nanocomposites in thermotropic or lyotropic liquid crystals and CNTs.[35–40] In liquid crystals, the effect of carbon nanotubes on the phase ordering of LC/CNT composites depends on the surface coupling of the LC molecules to the graphene-like surface, as well as the wrapping distribution with the radius of curvature of those surfaces. Such composites have been proposed as memory devices by exploiting their nanoelectromechanical properties.[43] Recently, investigations on LC/CNT composites have shown that the CNTs can induce chirality in the bulk LC.[44–46] Most of these studies were focused on nematic and smectic LC ordering and the phase transition behavior in LC/CNT composites. In all of these studies, a fundamental requirement is that nanotubes can be well dispersed and preferably also aligned in the composite, and that the nanotubes interact strongly with the surrounding LC matrix. As a results, the alignment of nanotubes is far from trivial and scale-up is challenging.

In this work, we turn to a liquid crystal host somewhat different than in previous studies. Here we study the phase transition behavior of the liquid crystal alkoxyphenylbenzoate (9OO4) doped with multiwall carbon nanotubes as a function of CNT concentration. Unlike the bulk of previous studies in which positive dielectric anisotropy liquid crystals of typically biphenyls with a limited phase sequence served as the host, here we examine a negative dielectric anisotropy phenylbenzoate whose core interacts differently with the CNT's graphene-like sheets. Moreover, 9OO4 allows us to study the full range of phases with one mesogen, including isotropic, nematic, smectic-A, and smectic-C. These features facilitate comparisons with the existing literature, and allow us to draw more detailed conclusions about how CNTs interact with the host mesogens. The incorporation of CNTs in 9OO4 reveals that all observed mesophase transition temperatures and the crystallization transition temperatures shift upward. This result suggests that the interactions between molecular structure, LC dipole moment, and graphene-like surface can allow the random dispersion of CNTs to promote both orientational and positional order. We interpret this effect in terms of an orientational ordering of the director at the CNT surface with a bulk-like order parallel to the CNT long axis over distances that span multiple nematic domains, while allowing the LC molecule to hop along the surface, accommodating various positional orderings. Our conjectured mechanism for 9OO4/CNTs is in contrast to a disordering mechanism for octyl cyanobiphenyl (8CB)/CNT mixtures.[31]

Our presentation is organized as follows: Section II describes the preparation of the sample and modulated differential scanning calorimetry procedure, as well as the electroclinic procedure; Sec. III describes the calorimetric and electroclinic results of all phase transitions in the 9OO4/CNT system; Sec. IV provides a discussion; and Sec. V provides conclusions of our work and future directions.

II. METHODOLOGY

A. Material and sample preparation

The liquid crystal 9OO4 is a phenyl benzoate containing an oxoester linkage group with two alkoxy end groups (see Figure 1). The molecular mass for 9OO4 is M_w = 424.7 g/mol with an extended molecular structure approximately 4 nm long and 0.8 nm wide. For 9OO4, modeling suggests that due to the carbonyl group, the effective dipole moment of 9OO4 is approximately perpendicular to the long axis and the average plane of the phenyl rings. Multi-wall CNTs were obtained from Nanostructured and Amorphous Materials, Inc. and have an average outer diameter of 8–15 nm, an inner diameter of 3–5 nm, a length of 500-2000 nm, and a distribution of different chiral structures.[44] To reduce aggregation, a small amount of CNTs was dispersed first in acetone and shaken for 30 min using a mixer, followed by sonication for 3 h. The 9OO4 was added to the acetone + CNT mixture to achieve the desired final weight percent ϕ_w of CNTs. The mixture then was sonicated for 3 h to facilitate dispersion. Finally, the acetone was evaporated slowly, then degassed under a modest vacuum in the isotropic phase of 9OO4 at ∼364 K (or 90°C) for about 2 h. Microbalance massing of the mixture was done to ensure complete removal of acetone before being sealed in the experimental cells. This process was repeated to

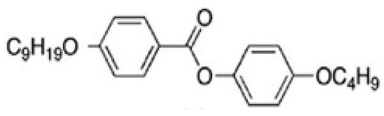

FIG. 1. The member of the 4-*n*-alkoxy phenyl-4′-*m*-alkoxy benzoate homolog series denoted *n*OO*m*. In this study, $n = 9$ and $m = 4$ (9OO4). Note that the negative dielectric anisotropy is due to the O–C=O group in the benzoate group linking the two phenyl rings. Molecular modeling suggests that the effective dipole moment of about 2.5 is pointing approximately perpendicular to the twisted phenyl rings, essentially out of the page.[58]

prepare 0 (pure 9OO4), 0.008, 0.010, 0.025, and 0.200 wt. % CNT calorimetry samples. All samples were tested with optical microscopy to see uniform dispersion of CNTs in LC system. On cooling, pure 9OO4 exhibits the phase sequence *I* – 87 – *N* – 73 – Sm*A* – 62 – Sm*C* – 50 – Sm*B* - 35 - *K* (crystal) whose structure is not known, where temperatures are in Celsius, while on heating melting occurs nearly 25 K higher, which is followed by a specific heat peak almost 2 K higher than the melting peak before the LC enters the Sm*A* phase. Further heating yields the N and I phases. Based on the imaginary specific heat $\Delta C_p''$ behavior, the *I*-*N* transition is weakly first-order, the *N*-Sm*A* is continuous, the Sm*A*-Sm*C* is continuous, the Sm*C*-Sm*B* is first-order, and the Sm*B*-*K* is strongly first-order. The initial melting from crystal is strongly first-order, followed by a second, weakly first order C_p feature that indicates the presence of a narrow temperature range having a smectic-like texture, as seen under polarizing microscopy (labeled Sm*X*) between the *K* and Sm*A* phase on heating.[47] Unfortunately, the polarizing microscope images could not identify which type of smectic is the Sm*X* region.

B. Modulated differential scanning calorimetry

Modulated (temperature) differential scanning calorimetry (MTDSC/MDSC) allows for the simultaneous measurement of the evolution of both the heat flow and heat capacity. It is essentially the combination of traditional ac-calorimetry with DSC. This method allows for measuring the total heat flow (enthalpy) as well as its non-reversible (kinetic or imaginary component) and the reversible (real component) heat capacities. A detailed description of the MDSC method can be found elsewhere.[48–54]

MDSC experiments were performed using a Model Q200 from TA Instruments, USA. Prior to all measurements, temperature calibration was done with a sapphire disc, under the same experimental conditions used for all 9OO4/CNT samples. The analysis method used to extract the complex specific heat is based on linear response theory.[48,55] In general, a temperature oscillation is described as $T(t) = T_0 + \dot{T}_0 t + A_T \sin(\omega t)$ where T_0 is the initial temperature at time $t = 0$, T is the absolute temperature at time t, $\dot{T}_0$ is the baseline temperature scan rate, A_T is the temperature amplitude, and ω ($\omega = 2\pi f$) is the angular frequency of the temperature modulation. The temperature rate is also time dependent and is given by $\dot{T}(t) = dT/dt = \dot{T}_0 + A_q \cos(\omega t)$ where A_q is the amplitude of the temperature modulation rate ($A_q = \omega A_T$). Since the applied temperature rate consists of two components, $\dot{T}_0$ the underlying rate and $A_q \cos(\omega t)$ the periodic rate, the measured heat flow *HF* also can be separated into two components in response to these rates. The periodic component can be described by $HF_Q = A_{HF} \cos(\omega t - \varphi)$, where A_{HF} is the amplitude of the heat flow and φ is the phase angle between heat flow and temperature rate. The absolute value of the complex specific heat is written as $C_p^* = A_{HF}/mA_q$ where m is the mass of the sample. The phase angle φ requires a small correction (calibration) to account for finite thermal conductivities of the sample and cell (see Ref. 54). The real (reversible) C_p' and imaginary (non-reversible) C_p'' parts of the specific heat are then given by

$$C_p' = C_p^* \cos(\varphi), \tag{1}$$

$$C_p'' = C_p^* \sin(\varphi), \tag{2}$$

which allow for a consistent definition of the complex specific heat. Typically, under equilibrium conditions, $C_p'' = 0$ after φ correction (or have a weak linear temperature dependence remaining). The appearance of a peak-like non-zero C_p'' feature commensurate with a peak in the real part of the specific heat indicates that this feature arises from a first-order transition and involves a latent heat, where the total heat capacity is given by $C_p = \sqrt{C_p'^2 + C_p''^2}$.

The excess specific heats were determined in order to isolate the contribution from the various transitions. A linear baseline was used over the entire temperature scan range in order to determine $\Delta C_p = C_p - C_{baseline}$ for both the real and imaginary components, though C_p'' always exhibited a very shallow linear baseline that was very close to zero, indicating near-equilibrium conditions for the experimental parameters used in this work. For specific heat features that are close together in temperature, the wing of one peak (usually the higher temperature peak) is subtracted from the lower specific heat peak in order to isolate the excess specific heat of the lower temperature transition, denoted as $\delta C_p = \Delta C_p - C_{wing}$, where for C_{wing} we used a mimic function (polynomial) for the underlying wing. This calculation was applied only to the real component of the specific heat.

The particular transition enthalpy component is simply the integration of the excess specific heat component over a consistent temperature range, e.g., $\Delta H' = \int \Delta C_p' dT$ for the real and $\Delta H'' = \int \Delta C_p'' dT$ for the imaginary enthalpy. The total magnitude of the transition enthalpy is defined as $\Delta H = \sqrt{(\Delta H')^2 + (\Delta H'')^2}$. Finally, for first-order transitions, the transition temperatures (T_{IN}, T_{CB}, T_{BK}, T_{KX}, and T_{XA}) are determined as the highest temperature of the two-phase coexistence region indicated by the onset of non-zero values of $\Delta C_p''$. For continuous transitions, the transition temperature is taken as the $\Delta C_p'$ peak temperature. Quasi-equilibrium parameters such as scan rate, temperature amplitude and modulation time period were determined varying their values until rate effects were minimized. However, the final parameters only approximate equilibrium conditions.

C. Electroclinic measurements

Details of the electroclinic effect experimental set up are described elsewhere.[56] Briefly, a cell of thickness $d = 7.7 \pm 0.1$ μm was constructed from a pair of indium-tin-oxide coated glass slides covered with a rubbed polyimide alignment layer. The cell was filled with 0.05 wt. % CNT in 9OO4, which aligned in the planar direction. Light polarized at 22.5° relative to the director orientation was incident on the cell, subsequently passing through the cell, an analyzer, and into a detector. On applying an ac electric field E at frequency $f = 25$ Hz across the cell, the director rotated in the cell's plane by an angle $\theta[\propto E]$, resulting in an ac intensity

component I_{ac} at frequency f, as measured by a lock-in amplifier. It can be shown[56] that the ratio $I_{ac}/4I_{dc}$ corresponds to the spatially averaged rms director rotation $\bar{\theta}$, where I_{dc} is the dc intensity measured at the detector. At each temperature the electric field was ramped from 0 to 2.6×10^6 V/m (rms) over a time 450 s, and the results were fitted to a straight line. The electroclinic coefficient is defined as $e_c \equiv d\bar{\theta}/dE$.

III. RESULTS

For the pure 9OO4, calorimetry shows that the *I*-*N* phase transition occurs at $T_{IN} = 86.23\,^{\circ}$C, the *N*-Sm*A* phase transition at $T_{NA} = 71.49\,^{\circ}$C, the Sm*A*-Sm*C* phase transition at $T_{AC} = 61.5\,^{\circ}$C, the Sm*C*-Sm*B* phase transition at $T_{CB} = 49.38\,^{\circ}$C, and Sm*B*-*K* phase transition at $T_{BK} = 35.3\,^{\circ}$C, in good agreement with literature values.[47] All the phase transitions are characterized by a distinct C_p peaks at a nearly equilibrium scan rate of ± 0.3 K/min (Figures 2–6). The strongly first-order melting followed by a second first-order C_p feature indicates the presence of an intermediate phase (labeled Sm*X*) between *K* and Sm*A* on heating. The transition temperatures and enthalpies of pure 9OO4 on cooling and heating are presented in Tables I and II.

For the *I*-*N* phase transition, the excess real specific heat signatures as a function of temperature about T_{IN} for pure 9OO4 and 9OO4/CNT composite samples are shown in Figure 2. The $\Delta C_p'$ of 9OO4/CNT for the *I*-*N* transition phase is steeper and narrower than in the pure 9OO4, with the peak maximum nearer the high-temperature side of the coexistence region. The $\Delta C_p'$ and C_p'' behaviors are consistent on heating and cooling, as well as being reproducible after multiple thermal cycles. The $\Delta C_p'$ wings above and below the *I*-*N* transition match each other and that of pure 9OO4 on heating and cooling. The $\Delta C_p'$ peak height for cooling and heating scans within the two-phase *I*+*N* coexistence region is about the same as that for pure 9OO4 up to $\phi_w \simeq 0.010$, decreasing markedly for the 0.025 sample, then rising with increasing ϕ_w up to the highest CNT content sample of 0.20 wt. % studied.

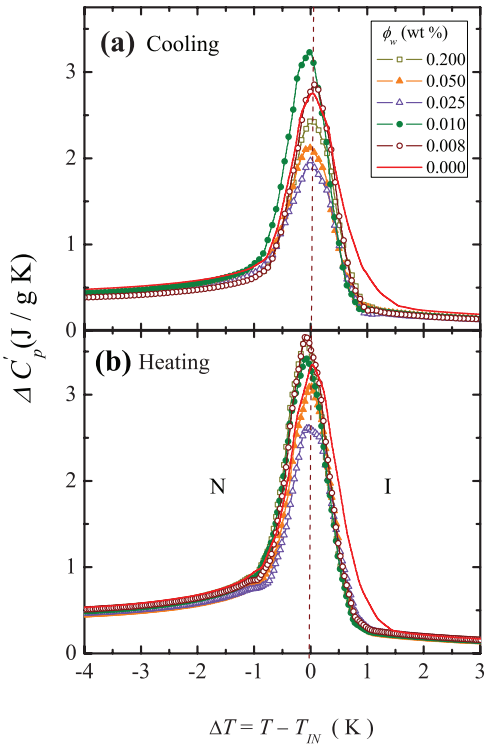

FIG. 2. (a) Excess real specific heat $\Delta C_p'$ associated with the *I*-*N* phase transition as function of temperature about T_{IN} on cooling. The definition of the symbols are given in the inset. (b) Excess real specific heat $\Delta C_p'$ associated with the *I*-*N* phase transition as function of temperature about T_{IN} on heating.

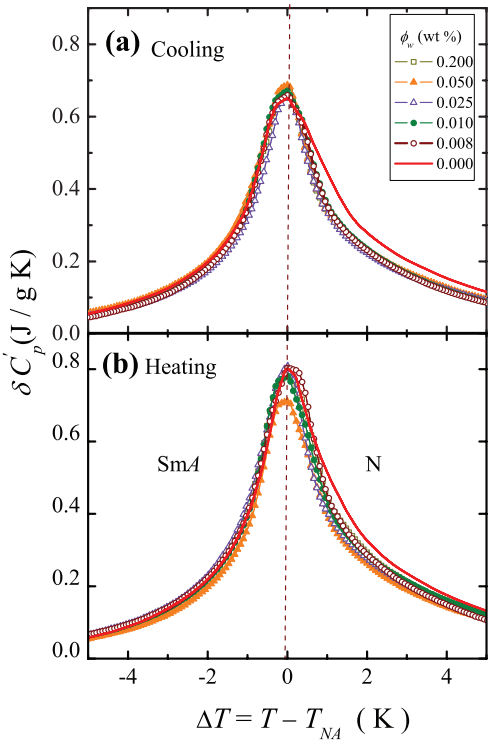

FIG. 3. (a) Excess real specific heat $\delta C_p'$ associated with the *N*-Sm*A* phase transition as function of temperature about T_{NA} on cooling. The definition of the symbols is given in the inset. (b) Excess real specific heat $\delta C_p'$ associated with the *N*-Sm*A* phase transition as function of temperature about T_{NA} on heating.

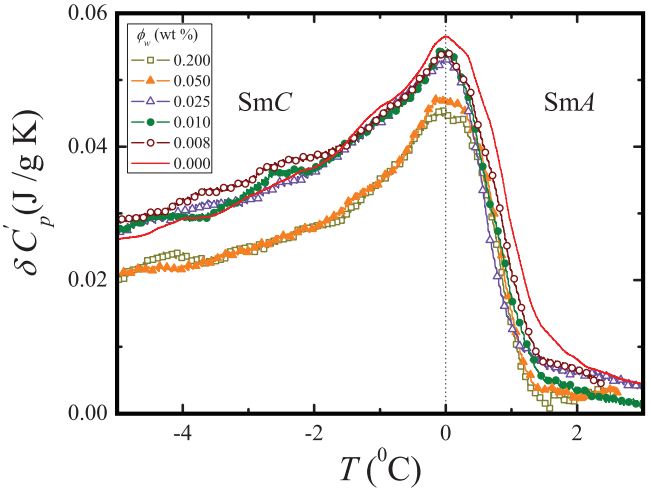

FIG. 4. Excess real specific heat $\Delta C_p'$ associated with the Sm*A*-Sm*C* phase transition as function of temperature about T_{AC} on cooling for different CNT content sample. The definition of the symbols is given in the inset.

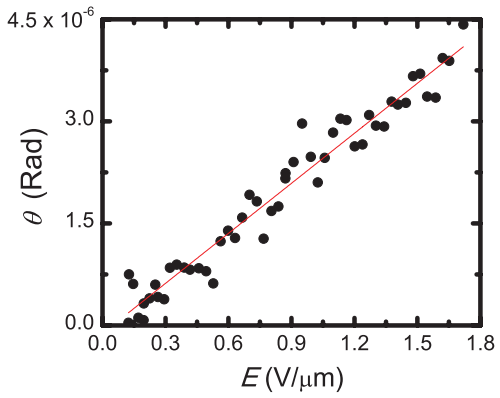

FIG. 5. Electroclinic response is a function of electric applied field (E). Data collected at temperature 63.2 °C, approximately 1.2 °C above Sm*A*-Sm*C* transition. Field was ramped over approximately 5 min.

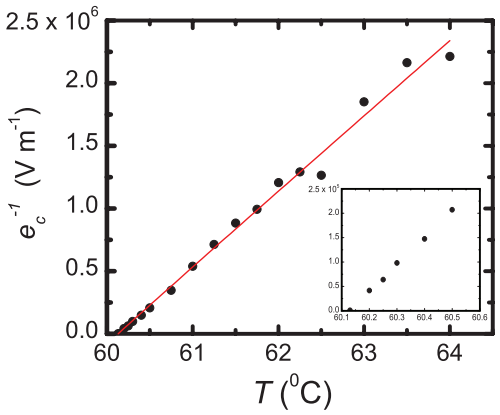

FIG. 6. The inverse electroclinic coefficient e_c^{-1} is shown as a function of temperature for an applied electric field at frequency 25 Hz across the cell containing a 0.05 wt. % 9OO4/CNT sample. The results were fitted a 3-parameter power law and resulted in a susceptibility exponent $\gamma = 0.99 \pm 0.06$. Inset shows an expanded view of the inverse electroclinic coefficient for low temperature range.

These small changes in $\Delta C_p'$ peak height may be arising from the uncertainty in measurements.

For the *N*-Sm*A* phase transition, the excess specific heat $\delta C_p'$ on cooling and heating as a function of temperature about T_{NA} are shown in Figure 3 for pure 9OO4 and 9OO4/CNT composite samples. For all samples, the *N*-Sm*A* phase transition does not exhibit any feature in the imaginary specific heat, indicating an apparent absence of latent heat and a likely continuous transition. The $\delta C_p'$ of the *N*-Sm*A* transition for the 9OO4/CNT samples overlay each other for all ϕ_w and for pure 9OO4 on the Sm*A* side, while they are systematically below that of pure 9OO4 on the nematic side of the transition. This may be arising because the pure sample has a smaller defect density than the composites. Given no strong change in the $\delta C_p'$ behavior as a function of ϕ_w, no power-law fits were attempted.

For the Sm*A*-Sm*C* phase transition, the excess specific $\delta C_p'$ as a function of temperature for pure 9OO4 and 9OO4/CNT composite samples are shown in Figure 4. The observed shape and continuous nature of the $\delta C_p'$ peak for pure 9OO4 are consistent with a Landau (mean-field) second-order transition[30] with no observed signature in C_p''. The $\delta C_p'$(AC) for the 9OO4/CNT samples magnitudes are the same as pure 9OO4 up to 0.025 wt. % and then decrease for the 0.05 and 0.20 wt. % samples. The step in $\delta C_p'$(AC) on the Sm*C*-side below T_{AC} is 0.025 J/gK for all samples, independent of ϕ_w.

The tilt susceptibility at the Sm*A*-Sm*C* transition was examined by measuring the electroclinic effect[56] in the LC/CNT mixtures. In the past, it has been shown that there is a nonzero enantiomeric excess for these CNTs, as well as a net chirality for CNTs from four different manufacturers.[42] When dissolved in a liquid crystal, the CNT imparts a net chiral environment to the liquid crystal in the vicinity of the CNT surface.[45] On application of an electric field, a surface electroclinic effect is seen, which requires the presence of a chiral symmetry environment and in which the director rotates by an angle $\theta \propto E$. Because of the sufficiently high concentration of

TABLE I. Summary of the transition temperatures for pure 9OO4 and all 9OO4/CNT samples on cooling and heating. Shown are CNT weight percent ϕ_w, the *I*-*N* transition temperature T_{IN}, the *N*-Sm*A* transition temperature T_{NA}, the *K*-Sm*X* transition temperature T_{KX}, the Sm*X*-Sm*A* transition temperature T_{XA}, the Sm*A*-Sm*C* transition temperature T_{AC}, the Sm*C*-Sm*B* transition temperature T_{CB}, and the Sm*B*-*K* transition temperature T_{BK}. All temperatures are given in Celsius.

ϕ_w	T_{IN}	T_{NA}	T_{AC}	T_{CB}	T_{BK}
0.000	86.19 ± 0.20	71.27 ± 0.12	61.10 ± 0.00	49.38 ± 0.02	35.00 ± 0.02
0.008	87.13 ± 0.22	72.68 ± 0.13	62.49 ± 0.02	50.33 ± 0.03	39.16 ± 0.03
0.010	87.14 ± 0.18	72.69 ± 0.11	62.50 ± 0.02	50.26 ± 0.02	39.34 ± 0.02
0.025	87.37 ± 0.21	72.52 ± 0.14	62.53 ± 0.01	50.25 ± 0.03	39.66 ± 0.04
0.050	86.92 ± 0.22	72.50 ± 0.12	62.28 ± 0.02	50.17 ± 0.04	39.85 ± 0.02
0.200	86.88 ± 0.23	72.48 ± 0.15	62.27 ± 0.02	50.13 ± 0.04	39.56 ± 0.01
ϕ_w	T_{KX}	T_{XA}	T_{NA}	T_{IN}	
0.000	60.96 ± 0.13	63.55 ± 0.01	71.46 ± 0.12	86.48 ± 0.22	
0.008	61.36 ± 0.12	64.24 ± 0.02	72.72 ± 0.13	87.27 ± 0.21	
0.010	61.45 ± 0.14	64.34 ± 0.02	72.85 ± 0.11	87.63 ± 0.19	
0.025	61.49 ± 0.14	64.06 ± 0.03	72.45 ± 0.14	87.10 ± 0.23	
0.050	61.42 ± 0.12	64.00 ± 0.03	72.62 ± 0.12	87.35 ± 0.25	
0.200	61.37 ± 0.13	63.98 ± 0.01	72.51 ± 0.15	87.27 ± 0.22	

TABLE II. Summary of the transition enthalpies for pure 9OO4 and all 9OO4/CNT samples on cooling and heating. Shown are CNT weight percent ϕ_w, the *I*-*N* transition δH^*_{IN} real enthalpy, imaginary enthalpy $\delta H''_{IN}$, the *N*-Sm*A* transition enthalpy δH^*_{NA}, the *K*-Sm*X* total transition enthalpy ΔH_{KX}, the Sm*X*-Sm*A* total transition enthalpy ΔH_{XA}, the Sm*C*-Sm*B* total transition enthalpy ΔH_{CB}, and the Sm*B*-*K* total transition enthalpy ΔH_{BK}. All enthalpies are given in Joules per gram. Also shown are the cumulative sum of all total transition enthalpies ΔH_T on cooling (top set) and heating (bottom set).

ϕ_w	δH^*_{IN}	$\delta H''_{IN}$	δH^*_{NA}	ΔH_{CB}	ΔH_{BK}	ΔH_T
0.000	3.9 ± 0.4	0.95 ± 0.03	3.1 ± 0.05	35.9 ± 0.06	33.3 ± 0.05	80.2 ± 0.55
0.008	3.8 ± 0.2	0.99 ± 0.04	2.6 ± 0.06	38.9 ± 0.05	41.0 ± 0.07	84.1 ± 0.42
0.010	4.3 ± 0.4	0.96 ± 0.02	2.6 ± 0.07	39.7 ± 0.04	39.2 ± 0.05	84.4 ± 0.62
0.025	3.2 ± 0.3	0.69 ± 0.03	2.6 ± 0.08	29.1 ± 0.08	33.6 ± 0.08	70.1 ± 0.55
0.050	3.4 ± 0.2	1.01 ± 0.04	2.8 ± 0.09	31.2 ± 0.06	39.2 ± 0.08	72.4 ± 0.38
0.200	3.6 ± 0.3	1.03 ± 0.03	2.7 ± 0.08	27.4 ± 0.09	39.6 ± 0.11	70.0 ± 0.45
ϕ_w	ΔH_{KX}	ΔH_{XA}	δH^*_{NA}	δH^*_{IN}	$\delta H''_{IN}$	ΔH_T
0.000	72.0 ± 0.16	32.0 ± 0.06	3.0 ± 0.06	4.9 ± 0.3	0.98 ± 0.02	83.4 ± 0.32
0.008	69.2 ± 0.15	17.1 ± 0.04	2.9 ± 0.08	5.1 ± 0.2	0.90 ± 0.04	85.7 ± 0.40
0.010	67.4 ± 0.12	13.6 ± 0.03	2.9 ± 0.08	4.8 ± 0.4	0.99 ± 0.02	83.9 ± 0.54
0.025	67.8 ± 0.06	10.5 ± 0.04	2.9 ± 0.07	4.2 ± 0.3	1.04 ± 0.02	75.0 ± 0.48
0.050	61.9 ± 0.08	10.3 ± 0.02	2.8 ± 0.06	4.4 ± 0.2	0.90 ± 0.03	85.3 ± 0.62
0.200	62.0 ± 0.08	12.7 ± 0.06	2.9 ± 0.09	5.0 ± 0.3	0.93 ± 0.03	74.6 ± 0.64

CNTs, the polarized light "sees" an average rotation $\bar{\theta}$ of the liquid crystal director for the entire sample. Figure 5 shows the director rotation at temperature 63.2 °C as a function of applied field.

The inverse electroclinic coefficient e_c^{-1} is shown as a function of temperature for the 0.05 wt. % 9OO4/CNT sample in Figure 6 approaching the Sm*C* phase from the Sm*A*. A three parameter (amplitude, T_{AC}, and susceptibility exponent γ) power-law fit of e_c^{-1} versus temperature resulted in $\gamma = 0.99 \pm 0.06$. Despite the localization of the chirality induced in the liquid crystal to within a few nanometers of the CNT surface,[57] the susceptibility exponent clearly is mean-field-like and apparently unaffected by the presence of the nanotubes aside from the chiral induction. This result suggests that the director rotation extends a length scale ξ, comparable to the Sm*C* correlation length, into the bulk liquid crystal from the narrow chiral region immediately surrounding the CNTs, which is the region that responds directly to the applied field. As an aside, we note that although T_{AC} was obtained for this non-zero concentration of nanotubes, it is not possible to compare it with the transition temperature in the absence of nanotubes, for which chirality would be absent and no electroclinic effect would be present.

For the Sm*C*-Sm*B*-*K* phase transition sequence on cooling, we show in Figure 7, the $\Delta C'_p$ and C''_p signatures for pure 9OO4 and 9OO4/CNT composite samples over a temperature range from +4 to −18 K about T_{CB}. All peak signatures remain sharp, while the peak height of the Sm*C*-Sm*B* phase transition decreases with increasing ϕ_w. The Sm*C*-Sm*B* transition is marked by a strongly first-order specific heat signature at $T_{CB} = 49.38$ °C, with the imaginary part being much larger than the real part. The total transition enthalpy ΔH_{CB} decreases slightly, whereas ΔH_{BK} increases slightly with increasing ϕ_w. Similarly, the imaginary part is much larger than the nearly non-existent $\Delta C'_p$ for the Sm*B*-*K* transition. This is consistent with both the Sm*C*-Sm*B* and Sm*B*-*K* phase transitions being strongly first-order, as expected. Note that the C''_p behavior observed in the Sm*B* phase is due to a very slow phase conversion to the Sm*B* from the Sm*C*.

For all samples, upon heating under continuous quasi-equilibrium conditions, the crystal phase superheats slightly until a strongly first-order specific heat feature is observed. Upon further heating, a second first-order feature is seen before the Sm*A* phase appears. See Figure 8 for pure 9OO4 and 9OO4/CNT composite samples over a range from −6 to +6 K

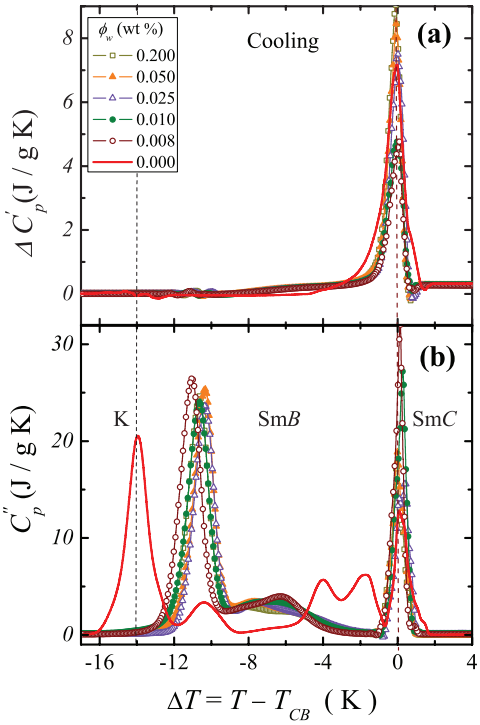

FIG. 7. (a) Excess real specific heat $\Delta C'_p$ associated with the Sm*C*-Sm*B* phase transition as function of temperature about T_{CB} on cooling. The definition of the symbols is given in the inset. (b) Imaginary specific heat C''_p as function of temperature about T_{CB} on cooling.

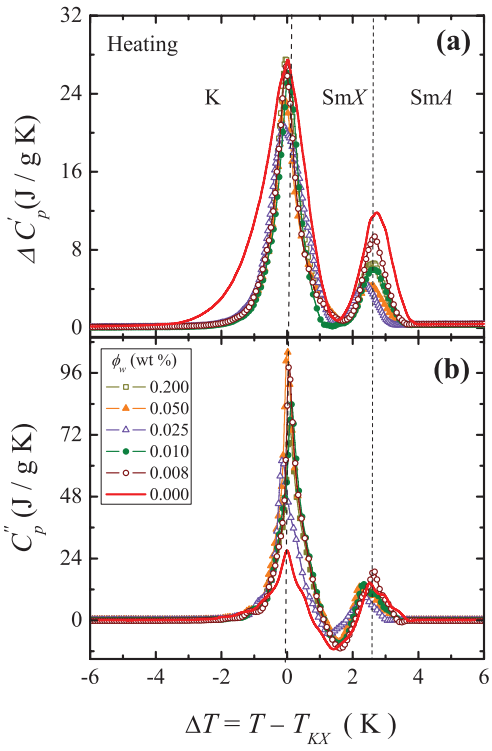

FIG. 8. (a) Excess real specific heat $\Delta C_p'$ associated with the *K*-Sm*X*-Sm*C* phase transition as function of temperature about T_{XA} on heating. The definition of the symbols is given in the inset. (b) Imaginary specific heat C_p'' as function of temperature about T_{XA} on heating.

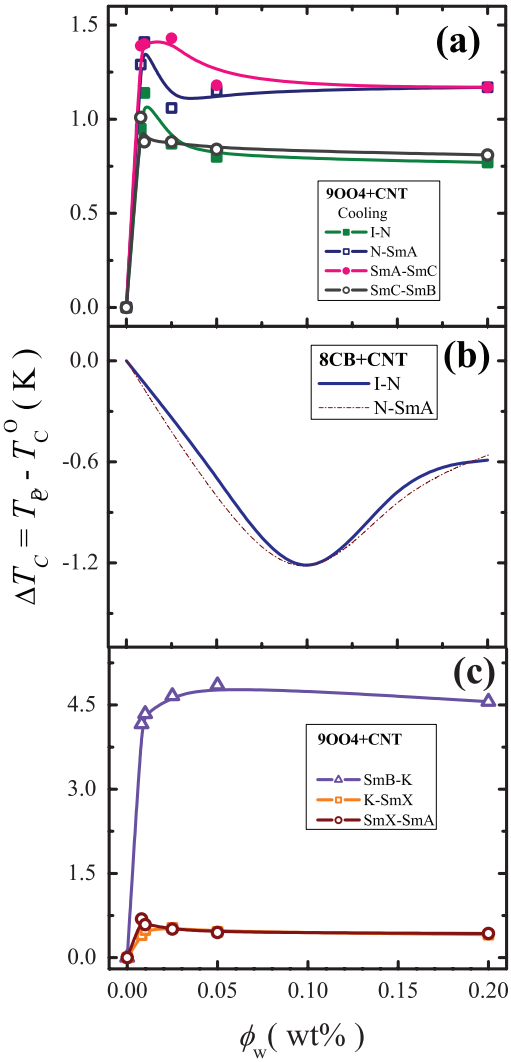

FIG. 9. (a) The phase transition temperature shifts for the *I*-*N* (■), *N*-Sm*A* (□), Sm*A*-Sm*C* (•), and Sm*C*-Sm*B* (○) in 9OO4/CNT samples and the *I*-*N* (−) and *N*-Sm*A* (−. − . −) transition temperature shift for 8CB/CNT[31] as a function of ϕ_w. (b) The phase transition temperature shifts of the Sm*B*-*K* (△), K-Sm*X* (□) and Sm*X*-Sm*A* (○) for the 9OO4/CNT samples as a function of ϕ_w.

about T_{KX}. The *K*-Sm*X* $\Delta C_p'$ peak is narrower for composite samples, except for the $\phi_w = 0.025$ wt. % sample, as compared to the pure 9OO4. The melting $\Delta C_p'$ peak generally decreases in amplitude with an increase in the C_p'' peak. The total transition enthalpy of $\Delta H_{KX} \simeq 72$ J/g for pure 9OO4 decreases slightly with increasing ϕ_w for the 9OO4/CNT samples. $\Delta H_{XA} \simeq 32$ J/g and strongly decreases with ϕ_w. Interestingly, the height of the second feature specific heat peak decreases with increasing ϕ_w and suggests that this feature is not due to residual crystal melting. Because of the magnitude of the enthalpy involved, it is possible that this feature is a transition into an intermediate smectic phase before heating into the Sm*A* phase. We denote this phase as Sm*X* and it is unclear from polarizing microscopy image as to whether this phase is Sm*B* or Sm*C*-like, as the melting occurs very near T_{AC} on cooling.

While the calorimetric and electroclinic behaviors of the phases and phase transitions for the 9OO4/CNT samples clearly retain the character found in pure 9OO4, the phase boundaries change slightly due to the CNT. The transition temperature shifts for all 9OO4/CNT samples relative to pure 9OO4 are shown in Figure 9. On **cooling**, the *I*-*N* transition temperatures in the 9OO4/CNT samples shift upward by nearly a constant +1.18 K compared to that in pure 9OO4, while the two-phase *I*+*N* coexistence widths shrink with a constant of ∼1.5 K in 9OO4/CNT over this range of ϕ_w. For the *N*-Sm*A* transition, the temperature in 9OO4/CNT shifts upward by +1.31 K compared to pure 9OO4, shrinking the nematic temperature range $\Delta T_{nem} = T_{IN} - T_{NA}$ by ∼0.3 K for all ϕ_w. The Sm*A*-Sm*C* transition temperature in 9OO4/CNT shifts upward by about +1.4 K, widening the Sm*A* range by +0.4 K for all ϕ_w. The Sm*C*-Sm*B* transition temperature shifts upward by +1.01 K, widening the Sm*C* range slightly for all ϕ_w studied. Finally on cooling, the Sm*B*-*K* crystallization shifts upward by the largest amount, +4 K for all ϕ_w, narrowing the Sm*B* ranges by 3 K. On **heating**, the *K*-Sm*X* phase superheats an additional +0.4 K, similarly for the Sm*X*-Sm*A* phase compared to pure 9OO4 for all ϕ_w samples. T_{NA} on heating is +1.2 K and the T_{IN} is +0.8 K higher than in pure 9OO4, narrowing the nematic range ΔT_{nem} by 0.4 K, similar to that seen on cooling.

IV. DISCUSSION

It is useful to compare these results with another high-resolution phase transition study of the octylcyanobiphenyl (8CB)/CNT nanocomposites, which also used near equilibrium calorimetric conditions and identical mixing method of

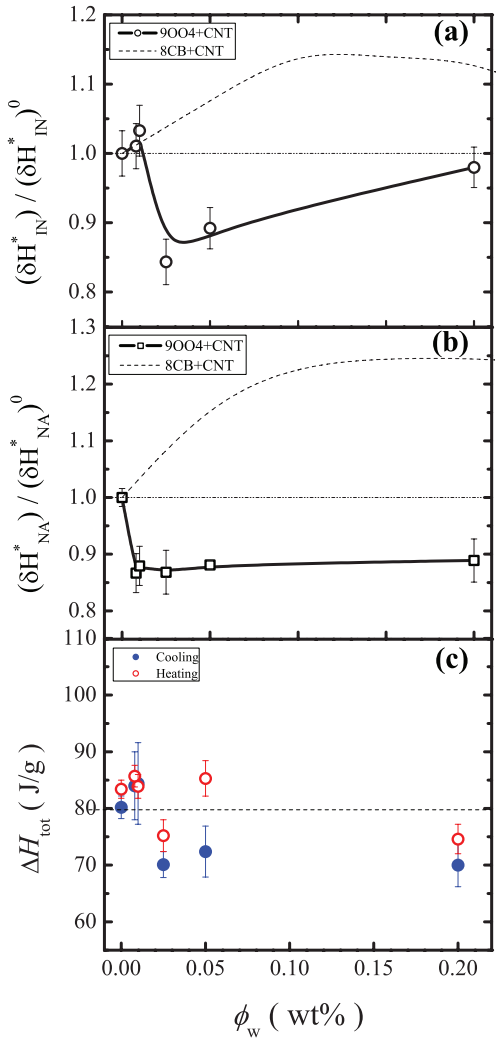

FIG. 10. (a) The *I*-*N* average fractional effective transition enthalpy for 9OO4/CNT (○) and 8CB/CNT (− − −) as a function of ϕ_w. (b) The *N*-Sm*A* average fractional effective transition enthalpy for 9OO4 (□) and 8CB (− − −) nanocomposites as a function of ϕ_w. (c) The effective total transition enthalpy on heating (○) and cooling (●) for the 9OO4/CNT samples as a the function of ϕ_w.

CNTs from the same source.[31] The 8CB is a typical rod-like molecule, with bi-phenyl core, to which are attached an aliphatic tail and a polar cyano head group, whereas 9OO4 has a benzoate group linking the two phenyl rings and has alkoxy end tails (see Figure 1). The transition temperatures and enthalpies of the isotropic to nematic and nematic to smectic-*A* phase transitions in 9OO4/CNT and 8CB/CNT systems[31] are shown in Figures 9 and 10. In the 8CB/CNT system, both transition temperatures shift downward by ∼1.5 K with increasing ϕ_w, with a non-linear ϕ_w dependence, while ΔT_{nem} remains constant, as seen by the solid and dashed-dotted lines in panel (a) of Figure 9. Apparently, the same surface distribution of CNTs for 8CB produces disordering effects of the orientational order, shifting both the *I*-*N* and *N*-Sm*A* transitions.

The transition enthalpies of the *I*-*N* and *N*-Sm*A* phase transitions in the 8CB/CNT system increase over a broad range of ϕ_w, and then remain constant for higher ϕ_w. The total transition enthalpy of the 8CB/CNT system has been interpreted as the sum of the pure transition contribution and a random-field induced distortion energy.[33] Apparently, given the near constant decrease of the enthalpy of the 9OO4/CNT, the orientational ordering is bulk-like with a reduction perhaps due to suppression of long-wavelength director fluctuations. If the enthalpy suppression of the *I*-*N* and *N*-Sm*A* in 9OO4/CNT were due to surface pinning, it would scale with CNT surface area, approximately linear in ϕ_w for these low concentrations, which is not observed. This suggests a different interaction for the 9OO4 than 8CB molecule with the CNT. The electroclinic effect results for 9OO4/CNT mixtures suggest that the director rotation extends a length scale ξ from the CNT surface, comparable to the Sm*C* correlation length, into the bulk liquid crystal, due to chiral induction immediately surrounding the CNTs. This chiral region can generate a bulk-like response to the applied field and result in a tilt over the entire Sm*C* correlation region. On cooling, the 9OO4/CNT Sm*B*-*K* phase transition temperature increases 4 K and *K*-Sm*X* phase transition temperature increases 0.5 K on heating for all ϕ_w while the total transition enthalpy remains constant on heating and cooling (see Figures 9 and 10). It is important to note that all experimental results presented here are reproducible over repeated scans.

From the calorimetric observations presented here, the effect of CNTs on the phase transitions of 9OO4 apparently enhances orientational order and is compatible with (at least) positional ordering of all the higher order phases, up to and including the crystal phase. This is despite the globally random dispersion of CNTs in these nanocomposites and in contrast to the disordering effects observed in the 8CB/CNT system.[31] Clearly, at such low concentrations with random CNT positional distributions, the CNT-LC boundary condition must play an important role along with the ultra-high average aspect ratio (130 ± 60) of the CNT nanoparticles.

To account for the opposite behaviors of the *I*-*N* transition for 9OO4/CNT and 8CB/CNT, given that the LC cores have very different chemical natures, the CNT may promote nematic order in both liquid crystals but with different extrapolation lengths (L = K/W) of the local anchoring field. For 8CB/CNT system, we conjecture that the LC orientations at the CNT surface can be quasi-random due to a degeneracy of possible orientations.[31] This would correspond to a small (100 nm) extrapolation length due to strong local anchoring and give rise to multiple domains on this length scale. As one domain moves outward from the CNT surface into bulk LC, these orientations would be uniform parallel to the CNT walls, but at the surface there would be some degree of quenched random-field disordering.[33] For the 9OO4/CNT system, there are only two possible LC orientations at the CNT surface and with larger extrapolation length. This would mean that the orientations at the CNT surface are more uniform and lead to a quenched locally-non-random field ordering. This is consistent with the observed ECE in 9OO4/CNT.[44,45] As a consequence in 9OO4/CNT, the local field would span multiple nematic domains and so actually suppress director fluctuations thereby promoting smectic ordering.

However, the observed enhancement of the higher order smectic phases as well as the crystal phase implies that the uniform surface orientational anchoring is not accompanied

by positional pinning along the CNT surface of the 9OO4 molecule. This degree of freedom of the LC molecule to essentially "hop" along the surface parallel to the CNT long-axis is needed to accommodate all the higher positional ordering (broken symmetries) in pure 9OO4 yielding the observed bulk-like behavior and phase boundary enhancement in this work. The origin of these two different behaviors for 9OO4 and 8CB with CNT dopant is not immediately known, but may be due either to the structure (the carboxyl) that gives rise to the negative dielectric anisotropy of 9OO4 as opposed to that in 8CB, or to the different commensurate surface packings of the phenyl rings onto the graphene surface by these two LCs.

V. CONCLUSIONS

We have presented a detailed calorimetric study on the effect of carbon nanotubes on phase transitions of 9OO4/CNT nano-composites as a function of CNT concentration. The complex specific heat was measured over a wide temperature range for negative dielectric anisotropy alkoxyphenylbenzoate liquid crystal (9OO4)/CNT composites as a function of CNT concentration. The thermal scans were performed under near-equilibrium conditions between 25 and 95 °C, first cooling followed by heating scans, for concentration of CNT ϕ_w ranging from 0 to 0.2 wt. %. All mesophases have transition temperatures 1 K higher and a crystallization temperature 4 K higher than that of the pure 9OO4. The crystal phase superheats until a strongly first-order specific heat feature is observed, indicating melting 0.5 K higher than in the pure 9OO4. The enthalpy change associated with I-N and N-Sm*A* phase transitions is only slightly changed with increasing ϕ_w, but is generally lower than pure 9OO4. The total transition enthalpy associated with the all transitions is independent on the CNT concentration and thermal treatment. The bulk-like behavior of the phase transitions is supported by the bulk-like 9OO4 ECE behavior of the Sm*A*-Sm*C* for the 0.05 wt. % sample. We speculate that these results arise from the LC-CNT surface interaction breaking orientational symmetry uniformly over a distance along the CNT greater than the nematic correlation length, but allowing the LC to slide or hop nearly freely on the CNT surface to accommodate various translational symmetries, leading to a net ordering effect for all transitions. These results suggest that the interactions between molecular structure, dipole moment of liquid crystal, and graphene-like surface can allow a random dispersion of CNTs to promote both orientational and positional order, depending on the length scale of the ordering and the degree of surface freedom. These effects of incorporating CNTs with LC are likely due to coupling between CNT and LC, the change in the elastic properties of composites and thermal anisotropic properties of CNT. Continued experimental efforts probing the homogeneity of the sample, frequency-dependent dynamics, smectic structures via x-ray scattering, and elastic behavior via light-scattering of the homogeneous sample as a function of CNT concentration and temperature would be particularly important and interesting.

ACKNOWLEDGMENTS

The authors are grateful to Robert P. Lemieux for providing the 9OO4 liquid crystal. This work was supported at WPI by the Department of Physics and a grant from the NSF Award No. DMR-0821292(MRI). At CWRU, this work was supported by the National Science Foundation's Condensed Matter Physics and Solid State and Materials Chemistry Programs under Grant No. DMR-1065491. At USNA, this work was supported by the Office of Naval Research under Grant No. N001613WX20992.

[1] S. Iijima, Nature (London) **354**, 56 (1991).
[2] E. T. Thostenson, Z. F. Ren, and T. W. Chou, Compos. Sci. Technol. **61**, 1899 (2001).
[3] J. N. Coleman, U. Khan, and Y. K. Gun'ko, Adv. Matter **18**, 689 (2006).
[4] J. N. Coleman, U. Khan, W. J. Blau, and Y. K. Gun'ko, Carbon **44**, 1624 (2006).
[5] F. H. Gojny, M. H. G. Wichmann, B. Fiedler, I. A. Kinloch, W. Bauhofer, A. H. Windle, and K. Schulte, Polymer **47**, 2036 (2006).
[6] Z. Ounaies, C. Park, K. E. Wise, E. J. Siochi, and J. S. Harrison, Compos. Sci. Technol. **63**, 1637 (2003).
[7] R. Haggenmueller, C. Guthy, J. R. Lukes, J. E. Fischer, and K. I. Winey, Macromolecules **40**, 2417 (2007).
[8] A. R. Bhattacharyya, T. V. Sreekumar, T. Liu, S. Kumar, L. M. Ericson, R. H. Hauge, and R. E. Smalley, Polymer **44**, 2373 (2003).
[9] E. Assouline, A. Lustiger, A. H. Barber, C. A. Cooper, E. Klein, E. Wachtel, and H. D. Wagner, J. Polym. Sci., Part B: Polym. Phys. **41**, 520 (2003).
[10] J. K. W. Sandler, S. Pegel, M. Cadek, F. H. Gojny, M. V. Es, J. Lohmar, W. J. Blau, K. Schulte, A. H. Windle, and M. S. P. Shaffer, Polymer **45**, 2001 (2004).
[11] P. Potschke, T. D. Fornes, and D. R. Paul, Polymer **43**, 3247 (2002).
[12] S. B. Kharchenko, J. F. Douglas, J. Obrzut, E. A. Grulke, and K. B. Migler, Nat. Matter **3**, 564 (2004).
[13] P. Poncharal, Z. L. Wang, D. Ugarate, and W. A. de Heer, Science **283**, 1513 (1999).
[14] L. Wang and Z. M. Dang, Appl. Phys. Lett. **87**, 042903 (2005).
[15] X. C. Zhang, B. S. Xu, H. D. Wang and Y. X. Wu, J. Appl. Phys. **100**, 113524 (2006).
[16] G. L. Zhao, D. Bagayoko, and L. Yang, J. Appl. Phys. **99**, 114311 (2006).
[17] S. Sinha, S. Barjami, G. Iannacchione, A. Schwab, and G. Muench, J. Nanopart. Res. **7**, 651 (2005).
[18] O. Stephan, D. Taverna, M. Kociak, K. Suenaga, L. Henrard, and C. Colliex, Phys. Rev. B **66**, 155422 (2002).
[19] A. Madarhri, G. Pecastings, F. Carmona, and M. E. Achour, J. Microwave Optoelectron. **6**, 38 (2007).
[20] Y. Sato, M. Terauchi, Y. Saito, and R. Saito, J. Electron Microsc. **55**, 137 (2006).
[21] P. Potschke, S. M. Dudkin, and I. Alig, Polymer **44**, 5023 (2003).
[22] K. Ahmad, W. Pan, and S. L. Shi, Appl. Phys. Lett. **89**, 133122 (2006).
[23] R. H. Baughman, A. A. Zakhidov, and W. A. de Heer, Science **297**, 787 (2002).
[24] P. G. Collins and P. Avouris, Sci. Am. **283**, 62 (2000).
[25] A. Javey, Q. Wang, A. Urai, Y. Li, and H. Dai, Nano Lett. **2**, 929 (2002).
[26] R. Martel, T. Schmidt, H. R. Shea, T. Hertel, and P. Avouris, Appl. Phys. Lett. **73**, 2447 (1998).
[27] J. W. Goodby, M. A. Waugh, S. M. Stein, E. Chin, R. Pindak, and J. S. Patel, Nature **337**, 449 (1989).
[28] S. Chandrashekhar, *Liquid Crystals* (Cambridge University Press, England, 1992).
[29] D. Demus, J. W. Goodby, G. Gray, H. Spiess, and V. Vill, *Handbook of Liquid Crystals* (Wiley-VCH, Canada, 1998).
[30] P. G. de Gennes and J. Prost, *The Physics of Liquid Crystals* (Oxford University Press, Clarendon, Oxford, England, 1993).
[31] K. P. Sigdel and G. S. Iannacchione, Eur. Phys. J. E **34**, 34 (2011).
[32] G. S. Iannacchione, S. Park, C. W. Garland, R. J. Birgeneau, and R. L. Leheny, Phys. Rev. E **67**, 011709 (2003).
[33] G. S. Iannacchione, Fluid Phase Equilib. **222–223**, 177 (2004).
[34] H. Duran, B. Gazdecki, A. Yamashita, and T. Kyu, Liq. Cryst. **32**, 815 (2005).
[35] A. M. Somoza, C. Sagui, and C. Roland, Phys. Rev. B **63**, 081403(R) (2001).

[36]W. Song and A. H. Windle, Macromolecules **38**, 6181 (2005).
[37]W. Song, I. A. Kinloch, and A. H. Windle, Science **302**, 1363 (2003).
[38]S. Zhang and S. Kumar, Small **4**, 1270 (2008).
[39]H. Y. Chen, W. Lee, and N. A. Clark, Appl. Phys. Lett. **90**, 033510 (2007).
[40]H. Y. Chen and W. Lee, Opt. Rev. **12**, 223 (2005).
[41]R. Basu and G. S. Iannacchione, Phys. Rev. E **81**, 051705 (2010).
[42]R. Basu, K. A. Boccuzzi, S. Ferjani, and C. Rosenblatt, Appl. Phys. Lett. **97**, 121908 (2010).
[43]R. Basu and G. Iannacchione, J. Appl. Phys. **106**, 124312 (2009).
[44]R. Basu, C. L. Chen, and C. Rosenblatt, J. Appl. Phys. **109**, 083518 (2011).
[45]R. Basu, J. S. Pendery, R. G. Petschek, R. P. Lemieux, and C. Rosenblatt, Phys. Rev. Lett. **107**, 237804 (2011).
[46]R. Basu, C. Rosenblatt, and R. P. Lemieux, Liq. Cryst. **39**, 199 (2012).
[47]P. Kalakonda and G. S. Iannacchione, "Calorimetric and dielectric study of a negative dielectricanisotropy alkoxy-phenyl-benzoate liquid crystal" (unpublished).
[48]J. E. K. Schawe, Thermochim. Acta **260**, 1 (1995).
[49]N. J. Coleman and D. Q. M. Craig, Int. J. Pharm. **135**, 13 (1996).
[50]J. M. Hutchinson and S. Montserrat, J. Therm. Anal. **47**, 103 (1996).
[51]A. Hensel, J. Dobbertin, A. Boller, and J. E. K. Schawe, J. Therm. Anal. **46**, 935 (1996).
[52]B. Wunderlich, J. Therm. Anal. **48**, 207 (1997).
[53]S. R. Aubuchon and P. S. Gill, J. Therm. Anal. **49**, 1039 (1997).
[54]S. Weyer, A. Hensel, and C. Schick, Thermochim. Acta **304–305**, 267 (1997).
[55]J. E. K. Schawe, Thermochim. Acta **271**, 127 (1996).
[56]S. Garoff and R. B. Meyer, Phys. Rev. Lett. **38**, 848 (1977).
[57]R. Berardi, H. G. Kuball, R. Memmer, and C. Zannon, J. Chem. Soc., Faraday Trans. **94**, 1229 (1998).
[58]Molecular modeling was done using Avogadro: an open-source molecular builder and visualization tool. Version 1.XX. http://avogadro.openmolecules.net/.